Journal of Power Sources 196 (2011) 1920–1931

Contents lists available at ScienceDirect

Journal of Power Sources

journal homepage: www.elsevier.com/locate/jpowsour

Numerical assessment of dependence of polymer electrolyte membrane fuel cell performance on cathode catalyst layer parameters

Salih Obut[a,*], Erdogan Alper[b]

[a] TUBITAK Marmara Research Center, Energy Institute, TR-41470, Kocaeli, Turkey
[b] Chemical Engineering Department, Hacettepe University, TR-06800, Ankara, Turkey

ARTICLE INFO

Article history:
Received 30 July 2010
Received in revised form
20 September 2010
Accepted 9 October 2010
Available online 16 October 2010

Keywords:
Polymer electrolyte membrane fuel cell
Three-dimensional model
Computational fluid dynamics
Cathode catalyst layer
Spherical agglomerate

ABSTRACT

In this work, a three-dimensional, non-isothermal and two-phase computational fluid dynamics model of a proton exchange membrane (PEM) fuel cell with straight flow field channel is developed and validated. The model is used to predict the performance of the PEM fuel cell with changing parameters of the cathode catalyst layer which was usually assumed to be composed of spherical agglomerates. The effect of cathode catalyst layer parameters such as catalyst layer thickness, ionomer film thickness, agglomerate size and porosity, on the current density and power output of the PEM fuel cell is investigated. The numerical results reveal that competitive influence of resistances to transport of species, electron and proton within the cathode catalyst layer determines the performance of the PEM fuel cell in terms of area specific power density ($W\,cm^{-2}$) and mass specific power density ($kW\ g_{Pt}^{-1}$).

1. Introduction

In the last decade, proton exchange membrane (PEM) fuel cells have received considerable attention due to their high efficiency, low temperature operation range, scalability, compactness and low emissions [1,2]. However, there are many technical barriers that prevent complete commercialization of PEM fuel cells. Among these reduction of precious metal catalyst loading, reliability and stability of performance under variety of conditions and durability of fuel cell module components are the most important issues that significant research effort has been devoted [3–5]. Catalyst loading and reliability, stability and durability of PEM fuel cell modules may be improved by optimizing the design and operating conditions. This requires complete understanding of complex and coupled transport phenomena of mass, energy and current.

It is well known that the performance of the PEM fuel cells is strongly dependent on the electrodes, especially at the cathode. The critical component of the electrodes is the catalyst layers. The catalyst layers are typically composed of carbon, ionomer and platinum which are randomly dispersed within a porous matrix. This random structure makes it difficult to find the optimum catalyst layer composition as well as structure. However, a properly constructed mathematical model with advanced manufacturing techniques might help engineers to obtain the highest possible performance with minimum use of precious metal catalyst.

In the last decade, the agglomerate structure model for catalyst layers has received a lot of attention in modeling of the PEM fuel cells [6–12]. This is because of various experimental studies supporting the presence of agglomerates and modeling studies in which the prediction capability of the agglomerate model revealed [6,10–13]. Agglomerate model assumes that platinum supported carbon particles are grouped and bonded with ionomer to form the agglomerates. These agglomerates may also be surrounded by a thin ionomer film. The shape of the agglomerates is usually assumed to be spherical since the spherical agglomerate model is showed to be the realistic representative of catalyst layers [10]. For the spherical agglomerate model, the electrochemical reactions are usually modeled with well known internal effectiveness factor approach commonly used for heterogeneous reactions occurred in porous catalyst particles.

In the literature, various numerical parametric studies were presented for analyzing the effect of the cathode catalyst layer parameters on the PEM fuel cell performance [14–20]. To the best knowledge of the authors of this article, none of these studies are performed for non-isothermal, two-phase operation of a PEM fuel cell using three-dimensional geometry and spherical agglomerate model for cathode catalyst layer. However, in the PEM fuel cells three-dimensional transport effects on distribution of species concentration, temperature, etc., is not negligible. Hence, in this

* Corresponding author. Tel.: +90 262 677 2765; fax: +90 262 641 2309.
E-mail addresses: Salih.Obut@mam.gov.tr, sobut@hacettepe.edu.tr (S. Obut), ealper@hacettepe.edu.tr (E. Alper).

0378-7753/$ – see front matter © 2010 Elsevier B.V. All rights reserved.
doi:10.1016/j.jpowsour.2010.10.030

Nomenclature

E_A	activation energy ($J\,mol^{-1}$)
a_{agg}	active agglomerate surface area per unit volume of agglomerate (m^{-1})
t_{cat}	catalyst layer thickness (μm)
m_{Pt}	catalyst loading per unit MEA area ($mg_{Pt}\,cm^{-2}$)
C	concentration ($kmol\,m^{-3}$)
k_c	condensation rate coefficient (s^{-1})
J	current density ($A\,cm^{-2}$) or ($A\,mg_{Pt}^{-1}$)
ρ	density ($kg\,m^{-3}$)
D	diffusion coefficient ($m^2\,s^{-1}$)
σ_{e-xy}	diffusion layer electric conductivity in x- and y-direction ($S\,m^{-1}$)
σ_{e-z}	diffusion layer electric conductivity in z-direction ($S\,m^{-1}$)
r_{Pt}	effective catalyst surface area ratio
η_{eff}	effectiveness factor
σ	electric or proton conductivity ($S\,m^{-1}$)
n_d	electro-osmotic drag coefficient
k_e	evaporation rate coefficient ($Pa^{-1}\,s^{-1}$)
F	Faraday constant ($C\,mol^{-1}$)
h_c	heat of condensation of water ($J\,kg^{-1}$)
H_{O_2}	Henry's law constant for the dissolution of oxygen into the electrolyte ($Pa\,m^3\,kmol^{-1}$)
δ	ionomer film thickness (nm)
K	isotropic permeability (m^2)
k	isotropic thermal conductivity ($W\,m^{-1}\,K^{-1}$)
EW_M	membrane equivalent weight ($kg\,kmol^{-1}$)
M	molecular weight ($kg\,kmol^{-1}$)
η	over-potential (V)
P_{O_2}	partial pressure of oxygen (Pa)
K_{xy}	permeability in x- and y-direction (m^2)
K_z	permeability in z-direction (m^2)
r_{PtC}	platinum mass ratio on Pt|C catalyst
ε_0	porosity (volume fraction of voids) of fuel cell components
ΔH_{rxn}^{an}	reaction enthalpy for anode half reaction ($J\,kmol^{-1}\,K^{-1}$)
ΔH_{rxn}^{ca}	reaction enthalpy for cathode half reaction ($J\,kmol^{-1}\,K^{-1}$)
J_0	reference exchange current density ($A\,m^{-2}$)
k_{ORR}	reaction rate coefficient for oxygen reduction reaction ($m\,s^{-1}$)
S	source
s	saturation
γ_d	saturation exponent for diffusion coefficient correction
k_{dw}	sorption/desorption rate coefficient (s^{-1})
S_c	specific surface area of catalyst particles ($m^2\,g^{-1}$)
ε_{agg}	spherical agglomerate porosity (volume fraction of voids in the spherical agglomerates)
r_{agg}	spherical agglomerate radius (μm)
k_{xy}	thermal conductivity in x- and y-direction ($W\,m^{-1}\,K^{-1}$)
k_z	thermal conductivity in z-direction ($W\,m^{-1}\,K^{-1}$)
φ	Thiele modulus
α	transfer coefficient
u	velocity $\times$ component ($m\,s^{-1}$)
v	velocity y component ($m\,s^{-1}$)
w	velocity z component ($m\,s^{-1}$)
μ	viscosity ($kg\,m^{-1}\,s^{-1}$)
ε_{i-film}	volume fraction ionomer covering the spherical agglomerates
ε_i	volume fraction ionomer in the catalyst layer ($\varepsilon_{i-agg} + \varepsilon_{i-film}$)
ε_{i-agg}	volume fraction ionomer in the spherical agglomerates
ε_{sol}	volume fraction of solid phase
$\Re$	volumetric transfer current ($A\,m^{-3}$)
λ	water content ($kmol\,H_2O\,kmol^{-1}\,SO_3^-$)

Superscripts

CL	catalyst layer
DL	diffusion layer
eff	effective property
MP	mono-polar plate
ref	reference value

Subscripts

a	anode
C	carbon
c	cathode
dw	dissolved water
e	electric
i	ionomer
M	membrane
Pt	platinum
p	proton
sol	solid

study, a three-dimensional, non-isothermal and two-phase computational fluid dynamics model is used for systematic analysis of the performance of a PEM fuel cell by considering area specific and platinum mass specific polarization curves. In the model, ionomer film covered spherical agglomerate structure is used for the modeling of cathode catalyst layer.

2. Three-dimensional PEM fuel cell model

A typical PEM fuel cell consists of a five-layer membrane-electrode assembly (MEA) sandwiched in between two mono-polar plates (or two bi-polar plates in a stack) on which anode and cathode flow fields are grooved. A five-layer MEA contains two electrodes as anode and cathode separated by a proton conducting polymer electrolyte membrane (PEM). Each of these electrodes consists of a thin catalyst layer coated on one side of diffusion layer which serves as diffusion medium for transport of reactant and products as well as for transport of electrons.

In a typical PEM fuel cell operation, usually humidified hydrogen gas is supplied to anode flow channel which diffuses through anode diffusion layer until reaching the anode catalyst layer where protons (H^+) and electrons are formed at the catalyst surface. The protons are transferred through ionomer inside the catalyst layer and the membrane to the cathode catalyst layer and electrons are transferred through the external circuit to cathode catalyst layer. Meanwhile, humidified oxygen (or air) is fed to the cathode flow channel and oxygen reaches the cathode catalyst layer by diffusing through the cathode electrode. At the catalyst surface, protons, electrons and oxygen forms water. The net reaction in the PEM fuel cell is given by following reaction:

$$H_2 + \tfrac{1}{2}O_2 \rightarrow H_2O + \text{Heat} + \text{Electricity} \quad (1)$$

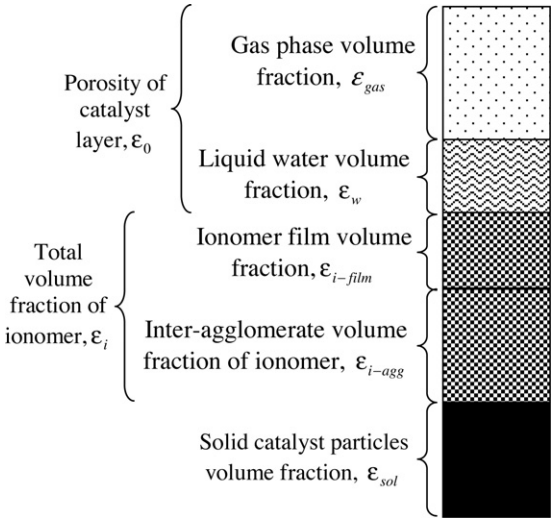

Fig. 1. Schematic representation of volume fraction of each phase in the PEM fuel cell catalyst layer.

2.1. Model assumptions

The following key assumptions are made: (a) steady-state, non-isothermal operation of PEM fuel cell is considered; (b) catalyst layers are assumed to be isotropic and homogeneous; (c) identical-sized, evenly dispersed spherical agglomerates are used to describe catalyst layers; (d) each spherical agglomerate is covered by a thin constant thickness ionomer film; (e) it is assumed that voids in the spherical agglomerates filled only with ionomer; (f) gases are assumed to be ideal, and gas flow is laminar; (g) water is produced in the ionomer phase of the cathode catalyst layer; (h) anisotropic properties, such as thermal conductivity, is considered for the diffusion layers; (i) fine mist flow is assumed for liquid water in gas channels.

2.2. Structure of the cathode catalyst layer

In the cathode catalyst layer solid, gas, liquid and ionomer volume fractions must be properly defined. In Fig. 1 volume fraction of each phase is shown schematically on unit catalyst layer volume.

The value of solid phase volume fraction (ε_{sol}) can be calculated using platinum loading (m_{Pt}), catalyst layer thickness (t_{cat}) and Pt|C ratio (r_{PtC}):

$$\varepsilon_{sol} = \left(\frac{1}{\rho_{Pt}} + \frac{1 - r_{PtC}}{\rho_C r_{PtC}}\right)\frac{m_{Pt}}{t_{cat}} \tag{2}$$

Ionomer volume fractions are given by

$$\varepsilon_{i-film} = \frac{\varepsilon_{sol}}{(1-\varepsilon_{agg})}\left[\left(1 + \frac{\delta}{r_{agg}}\right)^3 - 1\right] \tag{3}$$

$$\varepsilon_{i-agg} = \frac{\varepsilon_{sol}\varepsilon_{agg}}{1-\varepsilon_{agg}} \tag{4}$$

where ε_{agg} is the porosity or the volume fraction of voids between solid particles of the spherical agglomerates. The total ionomer volume fraction of the catalyst layer ε_i is simply the summation of ε_{i-film} and ε_{i-agg}. For two-phase operation gas phase volume fraction is obtained using liquid water saturation (s) and the dry porosity (ε_0) that is the volume fraction of voids in the porous layers

$$\varepsilon_{gas} = \varepsilon_0(1-s) \tag{5}$$

The active surface area of catalyst particles per unit agglomerate volume (a_{agg}) has to be known to calculate the volumetric transfer current in terms of catalyst volume. Thus following expression is used

$$a_{agg} = S_c r_{Pt}\frac{m_{Pt}}{t_{cat}}\frac{1}{(1-\varepsilon_0-\varepsilon_{i-film})} \tag{6}$$

where S_c is the specific surface area of the catalyst particles. Following correlation obtained from the data reported by the catalyst manufacturer E-TEK is used in the present model [21]

$$S_c = 7.401\times10^6 r_{PtC}^4 - 1.811\times10^7 r_{PtC}^3 + 1.545\times10^7 r_{PtC}^2 - 6.453\times10^6 r_{PtC} + 2.054\times10^6 \tag{7}$$

Specific area of the catalyst particles is multiplied by an effective surface area ratio (r_{Pt}) in order to take into account the isolation of active area [6,22].

2.3. Governing equations and source terms

The governing equations of the present model which are listed in Table 1 include conservation of mass, momentum, gas species (H_2, O_2 and H_2O), energy, electric and proton potentials, dissolved water and liquid water. All governing equations are listed in conservative form, appropriate for use in commercial flow solvers.

In the porous zones of the PEM fuel cell, effects of porosity and liquid water are taken into account in the source terms of Eqs. (9)–(11). Effective diffusion coefficients (D_j^{eff}) of individual species are calculated accordingly to include the effect of porous media, through Bruggemann's correction [6,12,23], and liquid water [24]:

$$D_j^{eff} = \varepsilon_{gas}^{1.5}(1-s)^{\gamma_d} D_j \tag{20}$$

where ε_g, s, γ_d and D_j are the gas phase volume fraction, liquid water saturation, saturation dependence exponent and diffusion coefficient of gas component j in gas mixture, respectively. In the gas channels, effective diffusion coefficient reduces to diffusion coefficient of component j in the gas mixture (D_j).

Consumption and production of gas species are defined in the source terms of species conservation equations (Eqs. (12)–(14)). Mass exchange of water between gas and liquid phases is included in the source term of Eq. (14) for catalyst and diffusion layers. In the catalyst layers source term also includes sorption/desorption of water. Conservation of energy is represented by Eq. (15) where heat source term (S_{th}) includes electrochemical reaction heat (S_{rxn}), ohmic heat (S_{ohm-e} and S_{ohm-i}) and phase change heat terms; condensation/evaporation (S_{lat}) and sorption/desorption (S_{sd}) heat sources. The heat of sorption/desorption was assumed to be equal

Table 1
Governing model equations.

Conservation equation	Conservative form	
Mass	$\nabla\cdot(\rho_g\vec{v}) = S_{mass}$	(8)
Momentum–x	$\nabla\cdot(\rho_g\vec{v}u) = -\partial P/\partial x + \nabla\cdot(\mu_g\nabla u) + S_{mom-x}$	(9)
Momentum–y	$\nabla\cdot(\rho_g\vec{v}v) = -\partial P/\partial y + \nabla\cdot(\mu_g\nabla v) + S_{mom-y}$	(10)
Momentum–z	$\nabla\cdot(\rho_g\vec{v}w) = -\partial P/\partial z + \nabla\cdot(\mu_g\nabla w) + S_{mom-z}$	(11)
Species–H_2	$\nabla\cdot(\rho_g\vec{v}Y_{H_2}) = \nabla\cdot(D_{H_2}^{eff}\nabla Y_{H_2}) + S_{sp.H_2}$	(12)
Species–O_2	$\nabla\cdot(\rho_g\vec{v}Y_{O_2}) = \nabla\cdot(D_{O_2}^{eff}\nabla Y_{O_2}) + S_{sp.O_2}$	(13)
Species–H_2O	$\nabla\cdot(\rho_g\vec{v}Y_{H_2O}) = \nabla\cdot(D_{H_2O}^{eff}\nabla Y_{H_2O}) + S_{sp.H_2O}$	(14)
Energy	$\nabla\cdot(\rho_g C_P\vec{v}T) = \nabla\cdot(k^{eff}\nabla T) + S_{th}$	(15)
Electric potential	$0 = \nabla\cdot(\sigma_s^{eff}\nabla\phi_e) + S_e$	(16)
Proton potential	$0 = \nabla\cdot(\sigma_p^{eff}\nabla\phi_p) + S_p$	(17)
Dissolved water	$0 = \nabla\cdot(D_{dw}\nabla C_{dw}) + S_{dw}$	(18)
Liquid water	$\nabla\cdot(\rho_L f(s)\vec{v}) = \nabla\cdot(\rho_L D_s\nabla s) + S_s$	(19)

to the latent heat of water evaporation/condensation [27]. Transports of electron and proton were modeled as in Eqs. (16) and (17) in which effective electric and proton conductivities were calculated using Bruggemann's type correction:

$$\sigma_e^{eff} = \varepsilon_{sol}^{1.5}\sigma_e \tag{21}$$

$$\sigma_p^{eff} = \varepsilon_i^{1.5}\sigma_p \tag{22}$$

In the present model, anisotropic electrical conductivity values are used for diffusion layers. Proton conductivity (σ_p) of ionomer phase in catalyst layers and the membrane were calculated using the expression given in the work of Springer et al. [25]

$$\sigma_p = (0.5139\lambda - 0.326)\exp\left[1268\left(\frac{1}{303} - \frac{1}{T}\right)\right] \quad \lambda > 1 \tag{23}$$

The conservation equation of dissolved water in the ionomer phase contains diffusion term and electro-osmotic drag terms, latter was included as a source term in Eq. (18). The diffusion coefficient of dissolved water in membrane is calculated using the correlation given by Motupally et al. [26]

$$D_{dw} = \begin{cases} 3.1\times10^{-7}\lambda(\exp(0.28\lambda)-1)\exp(-2346/T) & 0<\lambda\le 3 \\ 4.17\times10^{-8}\lambda(1+161\exp(-\lambda))\exp\left(-2346/T\right) & 3<\lambda<17 \end{cases} \tag{24}$$

Liquid water governing equation is given in Eq. (19) where viscous drag, capillary diffusion and phase change terms were included [22]. In the porous diffusion and catalyst layers, capillary pressure induced diffusion term dominates since viscous drag term is insignificant due to small gas velocities inside the porous media. Liquid water diffusivity, also called as capillary diffusivity, in Eq. (19) was calculated using [23]:

$$D_s = \frac{K_l}{\mu_l}\frac{dp_c}{ds} \tag{25}$$

where K_l is the liquid-phase permeability and p_c is the capillary pressure. Both are functions of liquid water saturation (s) and are defined as

$$K_l(s) = Ks^p \tag{26}$$

where K is the permeability of the porous media and the constant p takes the value of 3 for catalyst layers and 4.5 for diffusion layer [23]. In the literature, $p_c(s)$ function usually modeled using Leverett $J(s)$ function approach where Udell's empirical correlation used for $p_c(s)$ relationship [23]. However, this correlation is not appropriate to use in PEM fuel cell modeling since it is for sand/rock type porous media. Thus, in the present model experimentally determined capillary functions given by Ye and Nguyen [23] were used.

The source terms of all governing equations of the present model are indicated in detail with respect to PEM fuel cell components in Tables 2–4. Definition of each of the source terms given in Tables 2–4 is defined in Table 5.

The resistance to gas flow in diffusion and catalyst layers are given by Eqs. (27)–(29) and gas permeability correlation $(1-s)^p$ takes different exponents p as shown in Table 5 [23]. The expressions for consumption of hydrogen and oxygen and production of water are given in Eqs. (30)–(32). In the present model, water is assumed to be formed in the ionomer phase [27]. Ohmic heating (Eqs. (33) and (34)), electrochemical reaction heat source (Eq. (35)) and phase change source expressions (Eqs. (36) and (37)) are defined as in Table 5. The source terms of electric and proton potential equations (Eq. (38)) are calculated from the volumetric transfer current ($\Re$). For anode catalyst layer, the volumetric transfer current was calculated by using the Butler–Volmer equation:

$$\Re\left(A\,m^3\right) = (1-s)S_c r_{\mathrm{Pt}}\frac{m_{\mathrm{Pt}}}{t_{cat}}J_{0,a}^{ref}\left(\frac{C_{\mathrm{H_2}}}{C_{\mathrm{H_2}}^{ref}}\right)^{0.5} \times\left[\exp\left(\frac{\alpha_a F\eta_a}{RT}\right) - \exp\left(-(1-\alpha_a)\frac{F\eta_a}{RT}\right)\right] \tag{42}$$

where η_a is the anode over-potential defined as the difference between the electric and proton potentials:

$$\eta_a = \phi_e - \phi_p \tag{43}$$

For the cathode catalyst layer following expression was used to calculate the volumetric transfer current:

$$\Re\left(Am^3\right) = \frac{4F(1-s)(3/r_{agg})(\varepsilon_{sol}+\varepsilon_{i-agg})}{3/(\eta_{eff}a_{agg}k_{ORR}r_{agg}) + r_{agg}\delta/(D_{\mathrm{O_2}}(r_{agg}+\delta))}\frac{P_{\mathrm{O_2}}}{H_{\mathrm{O_2}}} \tag{44}$$

where the first term in the denominator represents the resistance due to diffusion and reaction inside the spherical agglomerates whereas the second term represents the resistance due to ionomer film surrounding the spherical agglomerates. Effect of blockage of active area by liquid water is modeled by the term $(1-s)$ in the numerator of Eq. (44) [28]. The internal effectiveness factor (η_{eff}) for the spherical agglomerates is given as follows [29]

$$\eta_{eff} = \left(\frac{1}{\varphi}\right)\left(\frac{1}{\tanh(3\varphi)} - \frac{1}{3\varphi}\right) \tag{45}$$

Table 2
Source terms of mass and momentum conservation equations.

	S_{mass}	S_{mom-x}	S_{mom-y}	S_{mom-z}
Anode				
Mono-polar plate	–	–	–	–
Flow channel	–	–	–	–
Diffusion layer	$-S_{phase}$	S_{m-x}	S_{m-y}	S_{m-z}
Catalyst layer	$S_{\mathrm{H_2}} - S_{phase} - S_{diss}M_{\mathrm{H_2O}}$	S_{m-x}	S_{m-y}	S_{m-z}
Membrane	–	–	–	–
Cathode				
Catalyst layer	$S_{\mathrm{O_2}} - S_{phase} - S_{diss}M_{\mathrm{H_2O}}$	S_{m-x}	S_{m-y}	S_{m-z}
Diffusion layer	$-S_{phase}$	S_{m-x}	S_{m-y}	S_{m-z}
Flow channel	–	–	–	–
Mono-polar plate	–	–	–	–

Table 3
Source terms of individual species and energy conservation equations.

	$S_{sp.\mathrm{H_2}}$	$S_{sp.\mathrm{O_2}}$	$S_{sp.\mathrm{H_2O}}$	S_{th}
Anode				
Mono-polar plate	–	–	–	S_{ohm-e}
Flow channel	–	–	–	–
Diffusion layer	–	–	$-S_{phase}$	$S_{ohm-e} + S_{lat}$
Catalyst layer	$S_{\mathrm{H_2}}$	–	$-S_{phase} - S_{diss}M_{\mathrm{H_2O}}$	$S_{ohm-e} + S_{ohm-i} + S_{rxn} + S_{lat} + S_{sd}$
Membrane	–	–	–	S_{ohm-i}
Cathode				
Catalyst layer	–	$S_{\mathrm{O_2}}$	$-S_{phase} - S_{diss}M_{\mathrm{H_2O}}$	$S_{ohm-e} + S_{ohm-i} + S_{rxn} + S_{lat} + S_{sd}$
Diffusion layer	–	–	$-S_{phase}$	$S_{ohm-e} + S_{lat}$
Flow channel	–	–	–	–
Mono-polar plate	–	–	–	S_{ohm-e}

Table 4
Source terms of electric potential, proton potential, dissolved water and liquid water conservation equations.

	S_e	S_p	S_{dw}	S_s
Anode				
Mono-polar plate	–	–	–	–
Flow channel	–	–	–	–
Diffusion layer	–	–	–	S_{phase}
Catalyst layer	$-S_{trn}$	$+S_{trn}$	$S_{diss}+S_{osm}$	S_{phase}
Membrane	–	–	S_{osm}	–
Cathode				
Catalyst layer	$+S_{trn}$	$-S_{trn}$	$S_{diss}+S_{osm}+S_{H_2O}$	S_{phase}
Diffusion layer	–	–	–	S_{phase}
Flow channel	–	–	–	–
Mono-polar plate	–	–	–	–

where φ is a dimensionless group known as Thiele modulus [29] for chemical reactions and for spherical particles it is defined as:

$$\varphi = \left(\frac{r_{agg}}{3}\right)\sqrt{\frac{a_{agg}k_{ORR}}{D_{O_2}^{agg}}} \tag{46}$$

where r_{agg} is the spherical agglomerate radius and a_{agg} corresponds the active area per unit agglomerate volume (Eq. (6)). In the model, it was assumed that the spherical agglomerates are porous; therefore, diffusion coefficient of the oxygen in the spherical agglomerates should be modified accordingly. In the present work, Bruggemann's correction is employed in the calculation of the effective inter-agglomerate diffusion coefficient of oxygen ($D_{O_2}^{agg}$)

$$D_{O_2}^{agg} = \varepsilon_{agg}^{1.5} D_{O_2} \tag{47}$$

where D_{O_2} is the diffusion coefficient of oxygen in the ionomer. The rate coefficient (k_{ORR}) for oxygen reduction reaction (ORR) is derived by writing the rate of reaction of oxygen in first order reaction rate form ($-r = k_{ORR}C_{O_2}$) and using Butler–Volmer type kinetics [6,14] for ORR

$$k_{ORR} = \frac{J_{0,c}^{ref}}{4FC_{O_2}^{ref}}\left[\exp\left(-\frac{\alpha_c F\eta_c}{RT}\right) - \exp\left((1-\alpha_c)\frac{F\eta_c}{RT}\right)\right] \tag{48}$$

where cathode over-potential (η_c) is given by

$$\eta_c = \phi_e - \phi_p - V_{OCV} \tag{49}$$

Open current voltage (V_{OCV}) of the PEM fuel cell was calculated using Eq. (50) correlated from the experimental data given by Parthasarathy et al. [30].

$$V_{OCV} = 0.002534T + 0.9251 \tag{50}$$

In Eq. (44), $C_{O_2}^{ref}$ represent the reference oxygen concentration at the conditions valid for the reference exchange current density ($J_{0,c}^{ref}$) of oxygen reduction reaction. The experimental data from the series of work published by Parthasarathy et al. [30,31] was used to correlate the reference exchange current density to temperature and used to evaluate the transfer coefficient. The transfer coefficient (α_c) was calculated depending on the operating voltage of the PEM fuel cell as follows:

$$\alpha_c = \begin{cases} 1 & V_{cell} \geq 0.8\,\text{V} \\ 0.495 + 2.3\times10^{-3}(T-300) & V_{cell} < 0.8\,\text{V} \end{cases} \tag{51}$$

In the diffusion and catalyst layers, water may condense and block the pores in the catalyst layer if water partial pressure exceeds the saturation pressure. The difference between saturation and partial pressure of water is taken as the driving force for the phase change. Thus, the phase change of water is modeled using the expression given in Eq. (39) where condensation (k_c) and evaporation (k_e) rates are assumed to be constant [32].

In catalyst layers, water may also dissolve into the ionomer phase according to water sorption equilibrium of the ionomer. The

Table 5
Definition of individual source terms.

Term	Expression	Note	
S_{m-x}	$-\frac{\mu_g}{K_x^i(1-s)^p}u$	$i=DL \rightarrow p=4.5$	
		$i=CL \rightarrow p=3$	(27)
S_{m-y}	$-\frac{\mu_g}{K_y^i(1-s)^p}v$	$i=DL \rightarrow p=4.5$	
		$i=CL \rightarrow p=3$	(28)
S_{m-z}	$-\frac{\mu_g}{K_z^i(1-s)^p}w$	$i=DL \rightarrow p=4.5$	
		$i=CL \rightarrow p=3$	(29)
S_{H_2}	$-\frac{\lvert\Re\rvert}{2F}M_{H_2}$		(30)
S_{O_2}	$-\frac{\lvert\Re\rvert}{4F}M_{O_2}$		(31)
S_{H_2O}	$+\frac{\lvert\Re\rvert}{2F}M_{H_2O}$		(32)
S_{ohm-e}	$\frac{i_{e-x}^2}{\sigma_{s-x}^{eff}}+\frac{i_{e-y}^2}{\sigma_{s-y}^{eff}}+\frac{i_{e-z}^2}{\sigma_{s-z}^{eff}}$	Reduces to i_e^2/σ_e^{eff} for isotropic medium	(33)
S_{ohm-i}	i_p^2/σ_p^{eff}		(34)
S_{rxn}	$\Re\left(\eta - \frac{T\Delta S}{nF}\right)$	$n=2$ for anode CL	
		$n=4$ for cathode CL	(35)
S_{lat}	$S_{phase}h_c$		(36)
S_{sd}	$S_{diss}M_{H_2O}h_c$		(37)
S_{trn}	$\Re$	Eq. 42 and 44	(38)
S_{phase}	$k_c\varepsilon_0(1-s)\frac{P_{wv}-P_{sat}}{RT}M_{H_2O}$ if $P_{wv}\geq P_{sat}$		
	$k_e\varepsilon_0 s(P_{wv}-P_{sat})\rho_{H_2O_{(l)}}$ if $P_{wv}<P_{sat}$	ε_0 is the dry porosity of the porous medium.	(39)
S_{diss}	$k_{dw}.(C_{dw}^{eq}-C_{dw})$		(40)
S_{osm}	$\nabla\cdot\left(n_d\frac{\sigma_p}{F}\nabla\phi_p\right)$		(41)

sorption/desorption of water is modeled using Eq. (40) where sorption/desorption rate constant k_{dw} is assumed to be 100 s^{-1} [27,33] in order to maintain near equilibrium conditions. The driving force for the sorption/desorption is the difference between equilibrium concentration of dissolved water in the ionomer phase and its actual value. In the dissolved water conservation equation, water transport due to electro-osmotic drag (Eq. (41)) is treated explicitly as a source term. In the present model, electro-osmotic drag coefficient (n_d) was taken as a linear function of water content (λ) of the polymer electrolyte [25]:

$$n_d = \left(\frac{2.5\lambda}{22}\right) \quad (52)$$

and the equilibrium water content of the ionomer and the membrane was modeled using the expression given by Hinatsu et al. [34]:

$$\lambda_{eq}(a) = 0.30 + 10.8a - 16.0a^2 + 14.1a^3 \quad (53)$$

where a is the relative humidity ($P_{H_2O}/P^{sat}_{H_2O}$) of the gas mixture. For relative humidity values larger than unity, the equilibrium water content is fixed to constant value of $\lambda_{eq}(1)$ by neglecting the Schroeder's Paradox since the absence of it has been illustrated [35].

2.4. Numerical methods

A single channel PEM fuel cell with straight flow channels on both anode and cathode sides was considered in this work. In the modeling, single domain approach [36] was used so that requirement of internal boundary conditions was avoided. In this approach, all of the governing equations solved numerically for all components of the PEM fuel cell. However, special treatments were applied to diffusion and convection terms in order to avoid the transport of dependent variable through the PEM fuel cell component on which dependent variable does not physically exist [23,36].

The governing mass, momentum, energy, charge, dissolved water and liquid water conservation equations were solved using the finite-volume technique. The commercial flow solver FLUENT® was utilized with its user defined function (UDF) feature by which charge, dissolved water and liquid water conservation equations were implemented. Diffusion coefficients and source terms of all conservation equations as well as all physical property definitions, correlations and geometrical definitions were incorporated by using custom written user defined C-language functions.

The SIMPLE algorithm [37] was used to handle the pressure–velocity coupling in the solution of continuity and momentum equations. Due to intrinsic non-linearity of the present model, the under-relaxation and the source term linearization techniques [37] were applied. Detailed grid dependence study was performed to maintain the solution time as low as possible while keeping the accuracy of the solution reasonable. For the present study, the total number of control volume was fixed to 95,040 for the half of the single channel geometry. The convergence criteria of 5×10^{-6} were used for the total residual of each conservation equation.

3. Results and discussion

3.1. Model validation

The three-dimensional model presented in preceding section validated against the experimental data reported by Chang et al. [38]. The MEA in the work of Chang et al. [38] has 50 cm^2 and has multi-channel serpentine flow field. In this study, one of the channels of the PEM fuel cell is considered. The cross flow between adjacent channels and the channel bends are neglected. Thus, straight and single channel fuel cell geometry with 25 cm length, as stated by Chang et al. [38] is used as model geometry. The fuel cell dimensions, MEA parameters and component properties used for the validation is taken either from the data given in Chang et al. [38] or taken from the literature and the manufacturer data (see Tables 6 and 7). Fig. 2 compares the polarization curve obtained from the present three-dimensional model and the experimental data. Over the whole range of experimental data, good agreement between numerical and experimental polarization curve is obtained. Small deviation between numerical and experimental polarization curves at high current densities may be attributed to neglected channel bends and cross-flow between the adjacent channels as well as parameter uncertainties.

Table 6
Key electrode parameters for baseline case.

Anode electrode parameters		
J_0	100 A m^{-2}	
α_a	0.5	
C_{ref}	0.59×10^{-3} kmol m^{-3}	[39]
r_{PtC}	0.2	
r_{Pt}	0.75	[6,22]
ε_i	0.59	
ε_0^{CL}	0.2	
ε_0^{DL}	0.74	[40]
Cathode electrode parameters		
$J_{0,LCD}$	1.3665×10^{-4} A m^{-2}	[30,31]
$J_{0,HCD}$	1.8694×10^{-2} A m^{-2}	[30,31]
$E_{A,LCD}$	73.3 kcal mol^{-1}	[30]
$E_{A,HCD}$	27.6 kcal mol^{-1}	[30]
C_{ref}	2.281×10^{-3} kmol m^{-3}	[30,31,39]
r_{PtC}	0.2	Baseline value
r_{Pt}	0.75	[6,22]
r_{agg}	0.3 μm	Baseline value
ε_{agg}	0.45	Baseline value
δ	85 nm	Baseline value
ε_0^{CL}	0.2	Baseline value
ε_0^{DL}	0.74	[40]

3.2. Analysis of cathode catalyst structure

After validating the present model with the experimental data, parametric analysis of cathode catalyst layer structure were performed in order to see the changes in area specific and platinum

Table 7
Properties and constants for baseline case.

Electrical properties of anode and cathode side fuel cell components		
σ_{xy}^{DL}	17241 S m^{-1}	
σ_z^{DL}	1250 S m^{-1}	
σ^{CL}	300 S m^{-1}	
σ^{MP}	20000 S m^{-1}	
K_{xy}^{DL}	1.3×10^{-11} m^2	[41]
K_z^{DL}	2.9×10^{-12} m^2	[41]
K^{CL}	3.0×10^{-14} m^2	[23]
Thermal properties of anode and cathode side fuel cell components		
k_{MP}	50 W m^{-1} K^{-1}	
k_{xy}^{DL}	11.0 W m^{-1} K^{-1}	[42]
k_z^{DL}	0.88 W m^{-1} K^{-1}	[42]
k_{CL}	0.27 W m^{-1} K^{-1}	[43]
k_M	0.16 W m^{-1} K^{-1}	[43]
Membrane properties		
ρ_M	1970 kg m^{-3}	
EW_M	1000 kg $kmol^{-1}$	
Additional constants		
ΔH_{rxn}^{an}	-226×10^3 J $kmol^{-1}$ K^{-1}	[44]
ΔH_{rxn}^{ca}	62.8×10^3 J $kmol^{-1}$ K^{-1}	[44]
k_c	100 s^{-1}	[32]
k_e	9.86×10^{-4} Pa^{-1} s^{-1}	[32]
k_{dw}	100 s^{-1}	[27]

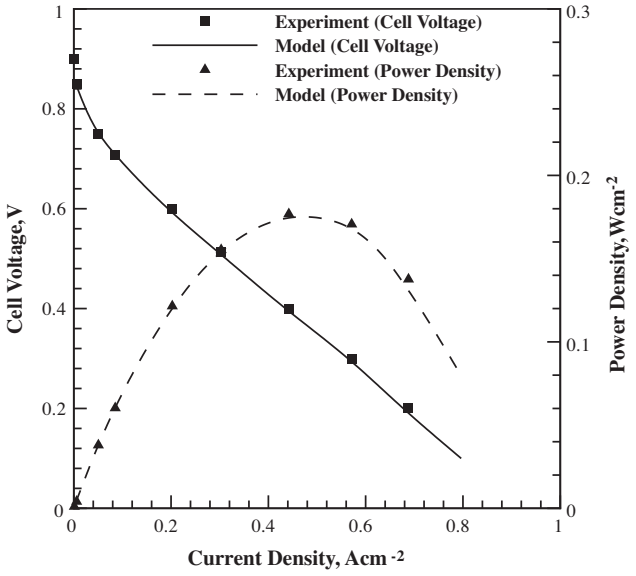

Fig. 2. Comparison of the model prediction with the experimental data reported by Chang et al. [38].

mass specific polarization and power density curves with changing cathode catalyst parameters. For this purpose a baseline case was prepared and its polarization curve was obtained by using the present model. The value of each cathode catalyst layer parameters is doubled or halved while keeping the remaining parameters constant. Polarization curves generated by the model were compared in order to investigate their effects on the PEM fuel cell performance. Following catalyst layer parameters were investigated in the present analysis:

- Platinum mass ratio of catalyst particles (r_{PtC}).
- Catalyst layer thickness (t_{cat}).
- Spherical agglomerate radius (r_{agg}).
- Agglomerate porosity (ε_{agg}).
- Ionomer film thickness around an agglomerate (δ).
- Catalyst layer porosity (ε_{cat}).

For the baseline case, single channel PEM fuel cell geometry is considered. Half of the cell geometry is used as computational domain by dividing it through the middle of the channel (Fig. 3). Same flow channel and diffusion layer dimensions are used for both side of the fuel cell. The geometrical dimensions are listed in Table 8. The operating conditions are as follows: fully humidified hydrogen gas and fully humidified air at 65 °C was fed into the anode and cathode sides, respectively. The temperature of anode and cathode terminals of the fuel cell was fixed to 65 °C. Anode and cathode channel back pressures were set to 152 kPa. The fuel cell electrode properties, fuel cell parameters and the operating parameters used in the baseline simulation are listed in Tables 6–7 and 9, respectively. The values of catalyst layer parameters used for parametric analysis are summarized in Table 10. Totally 13 polarization curves were generated during the simulations, each requiring runs for eight different operating voltages. In the subsequent sections, these polarization curves are compared and discussed in detail.

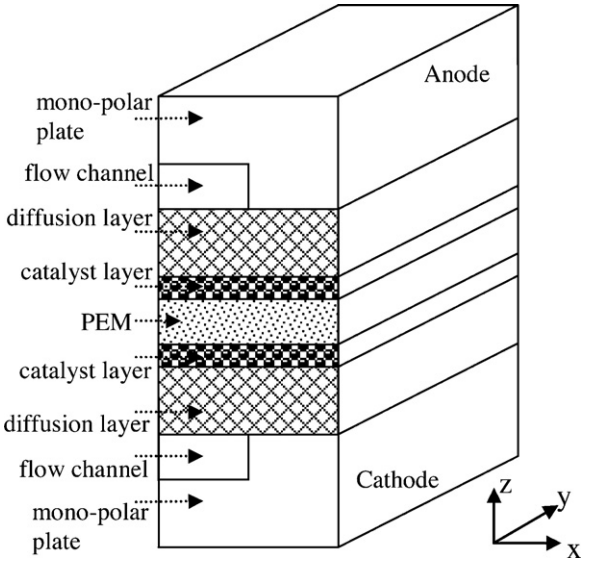

Fig. 3. Geometry of half of the straight channel PEM fuel cell used in this study.

Table 8
Geometric dimensions of the single channel PEM fuel cell.

Width[a]/height/length of flow channels	0.5 mm/1 mm/50 mm
Width[a] of flow channel spacing (shoulder)	0.5 mm
Thickness of diffusion layers	0.16 mm
Thickness of anode catalyst layer	0.02 mm
Thickness of cathode catalyst layers (baseline value)	0.04 mm
Thickness of membrane	0.04 mm
Thickness of mono-polar plates	1.2 mm

[a] The value corresponds to half of the fuel cell geometry.

Table 9
Operating parameters for baseline case.

Anode feed	
Stoichiometry at 1 A cm^{-2}	1.5
Mass flow rate	2.164×10^{-8} kg s^{-1}
Temperature	65 °C
Relative humidity	100%
Cathode feed	
Stoichiometry at 1 A cm^{-2}	2.0
Mass flow rate	3.998×10^{-7} kg s^{-1}
Temperature	65 °C
Relative humidity	100%
Anode/cathode terminal temperatures	65 °C
Anode/cathode side back pressures	152 kPa

3.2.1. Effect of platinum mass ratio of catalyst particles

The platinum mass ratio of catalyst particles determines the platinum loading of catalyst layer for constant values of other catalyst parameters. For r_{PtC} ratios of 0.1, 0.2 and 0.4, the platinum loadings of catalyst layer are approximately 0.46, 1.02 and 2.61 mg$_{Pt}$ cm^{-2}, respectively while volume fraction of solid, ionomer and gas phase as well as ionomer loading (2.2 mg cm^{-2}) are constant for all cases. In addition, increase of r_{PtC} ratio also decreases the specific active area of catalyst particles as indicated in Eq. (7). Thus, these two competitive effects determine the total active area per unit volume of catalyst layer that is proportional to catalyst r_{PtC} ratio for fixed catalyst layer thickness. Hence, the fuel cell performance is expected to be increased when r_{PtC} increased. Fig. 4 shows the polarization and the power curves obtained using the present model for platinum mass ratio of 0.1, 0.2 and 0.4. Considering the change of platinum loading, polarization and power curves (per unit area) of high r_{PtC} ratio case shifted upward while

Table 10
Cathode catalyst layer parameters used for parametric analysis.

	r_{PtC}	t_{cat} (μm)	r_{agg} (μm)	ε_{agg}	δ (nm)	ε_{cat}
Low value	0.1	20	1	0.15	25	0.1
Baseline	0.2	40	2	0.30	50	0.2
High value	0.4	80	4	0.60	100	0.4

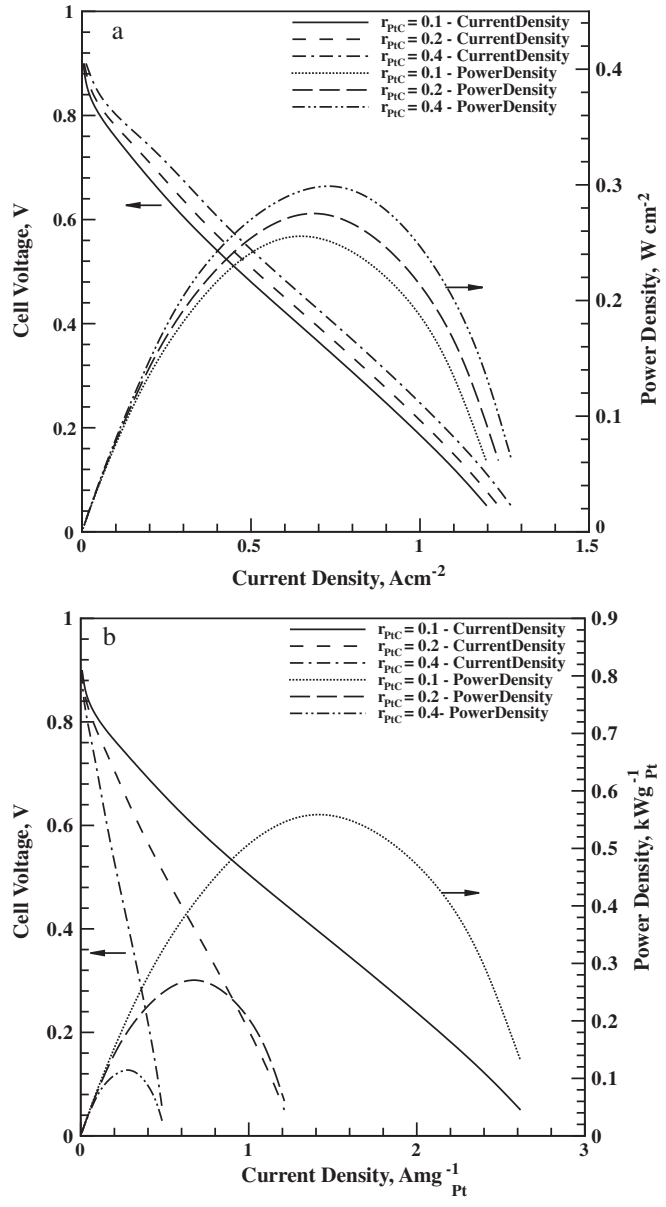

Fig. 4. Effect of platinum mass ratio of catalyst particles (r_{PtC}) on the fuel cell performance for t_{cat} = 40 μm, δ = 50 nm, r_{agg} = 2 μm, ε_{agg} = 0.3 and ε_{cat} = 0.2. (a) Polarization and power curves per unit MEA area and (b) polarization and power curves per unit platinum mass.

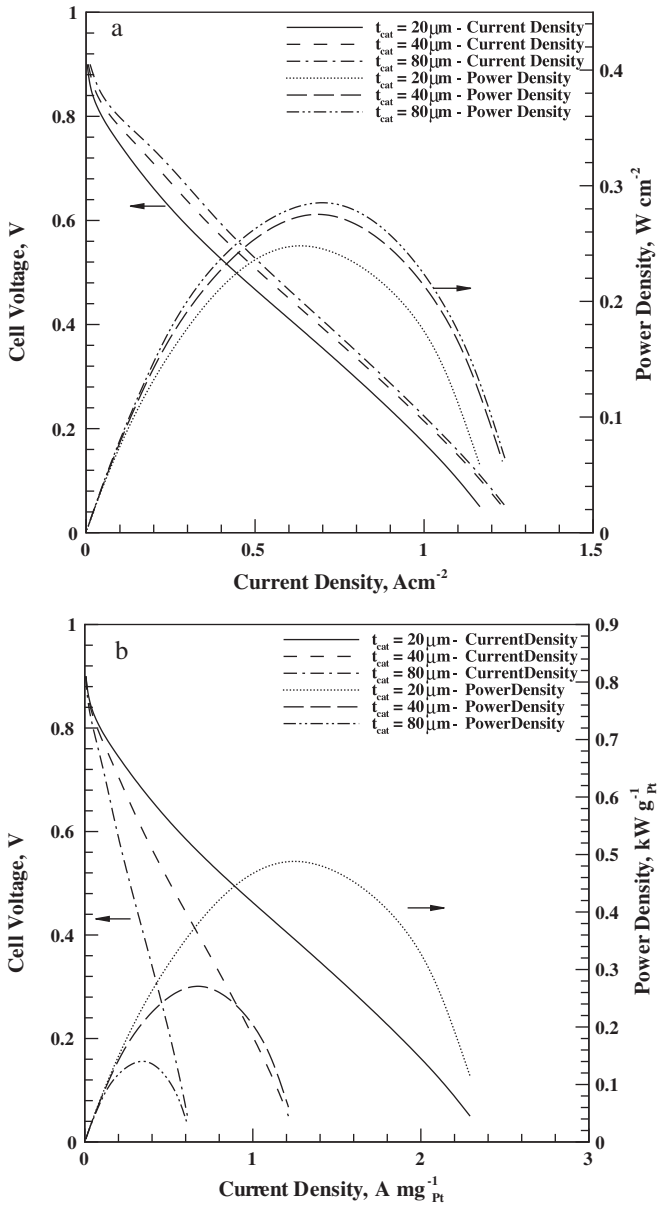

Fig. 5. Effect of catalyst layer thickness (t_{cat}) on the fuel cell performance for r_{PtC} = 0.2, δ = 50 nm, r_{agg} = 2 μm, ε_{agg} = 0.3 and ε_{cat} = 0.2. (a) Polarization and power curves per unit MEA area and (b) polarization and power curves per unit platinum mass.

that of low r_{PtC} ratio shifted downward (Fig. 4a). However, the current and power output from the fuel cell per unit mass of platinum shows inverse behavior so that better performance obtained for low r_{PtC} ratio (Fig. 4b). This implies that increase of platinum loading by r_{PtC} ratio may not be as favorable as expected in terms of effective utilization of the catalyst because of the decreasing specific surface area of catalyst particles. From the current analysis, the increase of r_{PtC} ratio results in higher area specific current and power densities for the range of parameters studied. However, the effective utilization of platinum loading was attained for low value of r_{PtC}.

3.2.2. Effect of catalyst layer thickness

Fig. 5 shows the polarization and power curves of simulations obtained by altering the catalyst layer thickness from its base value (40 μm) to 20 and 80 μm. The operating conditions as well as other catalyst parameters are kept constant. The direct effect of catalyst layer thickness is on platinum loading of catalyst layer of the fuel cell; the higher the catalyst layer thickness the larger the platinum loading of catalyst layer. From Fig. 5a, it is seen that for low current densities, area specific current and power output per unit area of cell increases with catalyst layer thickness. This is because of lower oxygen demand of the catalyst layer at low current densities resulting in excess amount of oxygen in the catalyst layer. Therefore, current density per unit area increases with t_{cat} at low current densities. However, at higher current densities >0.75 A cm^{-2} approximately the same area specific current density was observed for 40 and 80 μm. This implies that, the determining factor for power output from the fuel cell starts to become the limitation of mass transport inside the catalyst layer. At this point use of thicker catalyst layer is ineffective.

On the other hand, if current and power output of fuel cell compared on platinum mass basis (Fig. 5b), the thinnest catalyst layer (20 μm, ~0.51 mg$_{Pt}$ cm^{-2}) displayed better performance in terms of effective platinum usage whereas fuel cell performance in terms

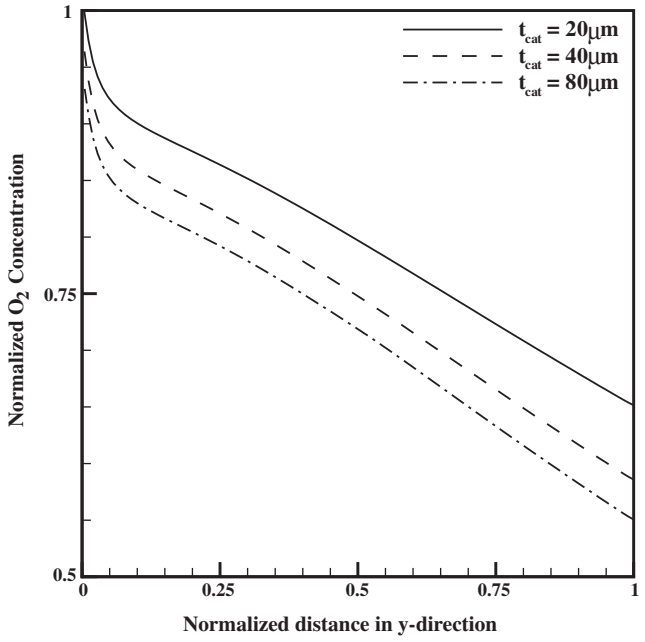

Fig. 6. Change of catalyst layer oxygen concentration along y-direction, at the middle of catalyst layer in x-direction and 10 μm away from the membrane at 0.4 V cell potential.

of per unit area is lower than its base case (t_{cat} = 40 μm). One of the major reasons for that is the resistance to oxygen transport in catalyst layer. In the thinnest cathode catalyst layer, average oxygen concentration in the cathode catalyst layer is expected to be higher. This is due to the shorter average transport length of oxygen from diffusion layer to catalyst active sites. This effect is clearly seen in Fig. 6, where the oxygen concentration along the channel direction (y-direction) is plotted for the same distance away the membrane. According to Fig. 6, the oxygen concentration along the channel is always larger for 20 μm thick catalyst layer. Another reason might be the decrease of cathode over potential because of the thin catalyst layer that means lower total resistance to proton transport. Consequently, for the range of interest, even though thicker catalyst layer resulted in higher current and power output per unit area, effective utilization of catalyst layer might be obtained by using thinner catalyst layer.

3.2.3. Effect of spherical agglomerate radius

In the spherical agglomerate model, as the agglomerate radius increases at constant catalyst thickness and porosity; solid volume fraction increases and ionomer volume fraction decreases as indicated by Eq. (3). Thus, platinum loading of catalyst layer and agglomerate radius are proportional. If the change of platinum loading with the agglomerate radius is considered, the performance of the cell should increase; however, in the present model, inter-particle effectiveness factor of spherical agglomerates are inversely proportional with r_{agg} as pointed in Thiele modulus (Eq. (46)). In addition, the increase of agglomerate radius also enhances electron transport by positive contribution to effective electrical conductivity of catalyst layer (Eq. (21)). At the same time, reduction in ionomer volume fraction adversely affects effective proton conductivity of catalyst layer so that effective proton conductivity of catalyst layer decreases (Eq. (22)).

Polarization and power curves for three different values of agglomerate radius are shown in Fig. 7. It is observed that current and power output per unit area and per unit platinum mass both increase with decreasing agglomerate radius. It is also observed that cell performance is influenced considerably by agglomerate inter-particle effectiveness factor. The effect can also be inferred

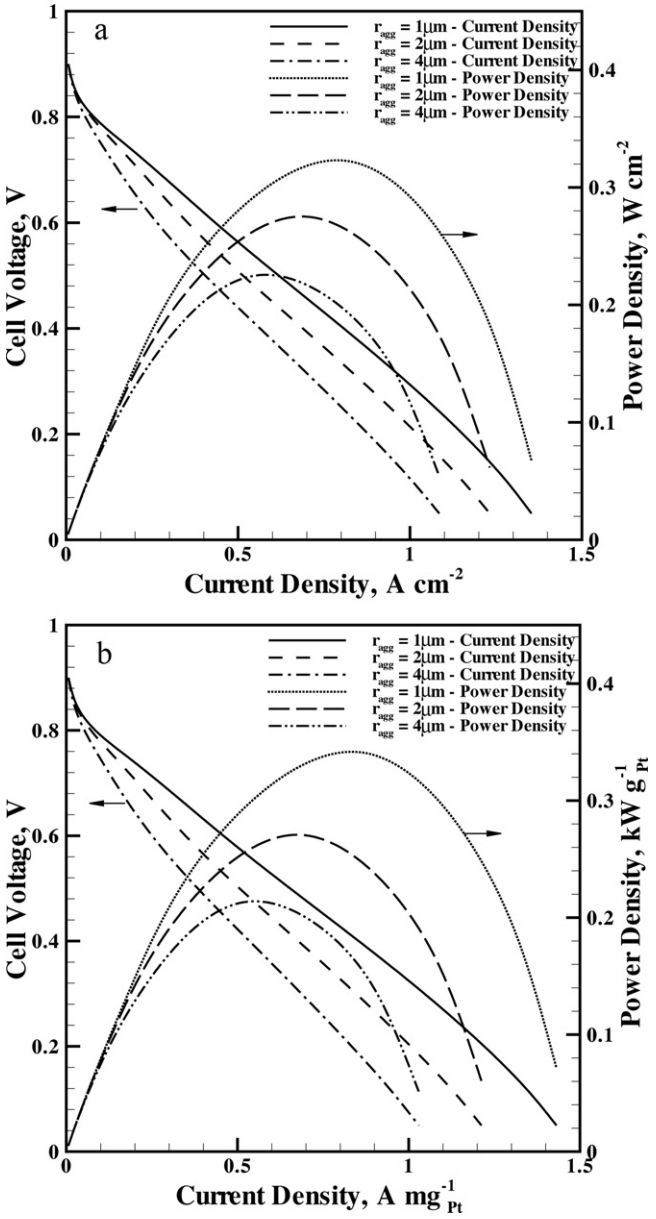

Fig. 7. Effect of spherical agglomerate radius (r_{agg}) on the fuel cell performance for r_{PtC} = 0.2, δ = 50 nm, t_{cat} = 40 μm, ε_{agg} = 0.3 and ε_{cat} = 0.2. (a) Polarization and power curves per unit MEA area and (b) polarization and power curves per unit platinum mass.

from volume average values of agglomerate inter-particle effectiveness factor, effective electrical and proton conductivity of cathode catalyst layer and average current density of the fuel cell. In Fig. 8, normalized values of these quantities are plotted against the agglomerate radius at 0.4 V cell potential. Fig. 8 indicates that, the effective electrical conductivity increases with r_{agg} and effective proton conductivity and inter-particle effectiveness factor have reverse trend. Besides, inter-particle effectiveness factor is found to be more sensitive to r_{agg} than the other parameters. Therefore, current analysis suggests that better cell performance might be obtained by increasing both the effectiveness factor and the effective proton conductivity by reducing the agglomerate radius, r_{agg}.

3.2.4. Effect of agglomerate porosity

In the present model, it was assumed that voids in the spherical agglomerates filled only with ionomer. The oxygen reaches the active reaction sites by diffusing through the ionomer. Thus, larger

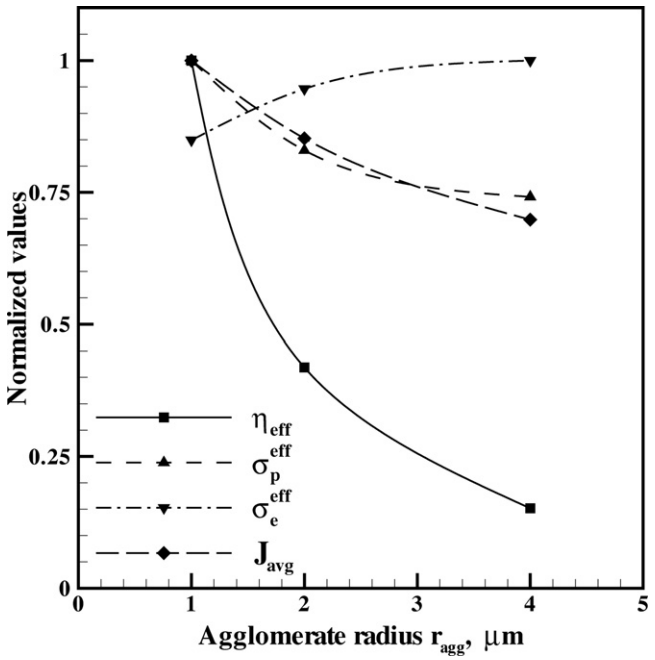

Fig. 8. Effect of agglomerate radius (r_{agg}) on normalized volume average values of inter-particle effectiveness factor (η_{eff}), effective electric and proton conductivity of catalyst layer (σ_e^{eff}, σ_p^{eff}) and average current density (J_{avg}) at 0.4 V cell potential for fixed values of r_{PtC} = 0.2, δ = 50 nm, t_{cat} = 40 μm, ε_{agg} = 0.3 and ε_{cat} = 0.2.

agglomerate porosity (ε_{agg}) promotes the oxygen diffusion inside the agglomerate by increasing the effective diffusion coefficient given by Eq. (47).

Fig. 9 shows the polarization and power curves for ε_{agg} varying from 0.15 to 0.6. The polarization curves in Fig. 9a show that the performance of the PEM fuel cell increases proportionally with ε_{agg}; however, at low current densities <~0.15 A cm^{-2} the performance of three cases are nearly the same and the lowest obtained when ε_{agg} is small. At high current densities, better performance observed for high value of ε_{agg}. The difference between the three cases might be the effect of proton conductivity of cathode catalyst layer that increases with ionomer fraction of the catalyst layer. The values of ionomer volume fractions of three cases conform the effect (ionomer volume fractions are 0.169, 0.280 and 0.503 for ε_{agg} of 0.15, 0.3 and 0.6, respectively). Therefore, it can be said that the PEM fuel cell performance is a strong function of the ionomer volume fraction and so the effective proton conductivity of the catalyst layer.

On the other hand, if the polarization curves were plotted in terms of platinum loading, the relationship between ε_{agg} and the cell performance become clearer. As shown in Fig. 9b, the cell performance improves with ε_{agg} for all current densities. This is mainly due to the fact that the platinum loading of the catalyst layer decreases with increasing ε_{agg} (Eqs. (2)–(4)). The reduction in proton transport resistance and platinum loading both increases the mass specific current and power output of the cell. In addition, increase of ε_{agg} is also beneficial for inter-particle diffusion of oxygen, since effective diffusion coefficient of oxygen inside the agglomerates gets higher with ε_{agg}, thereby increasing the inter-particle effectiveness factor defined in Eq. (45) by means of reducing the Thiele modulus Eq. (46). Therefore, higher current and power density (per unit area and per platinum loading) can be obtained by large values of ε_{agg}.

3.2.5. Effect of ionomer film thickness around an agglomerate

In the present agglomerate model, each one of the agglomerate is assumed to be covered with a constant finite thickness

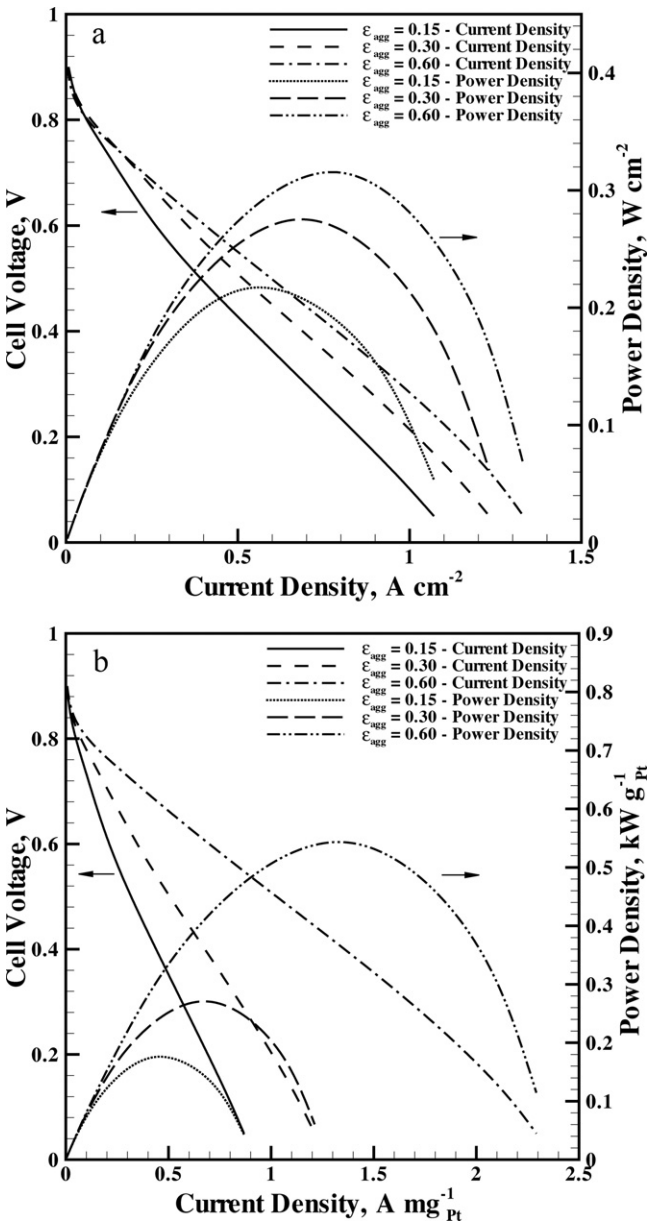

Fig. 9. Effect of agglomerate porosity (ε_{agg}) on the fuel cell performance for r_{PtC} = 0.2, δ = 50 nm, t_{cat} = 40 μm, r_{agg} = 2 μm and ε_{cat} = 0.2. (a) Polarization and power curves per unit MEA area and (b) polarization and power curves per unit platinum mass.

ionomer film. This ionomer film serves as a connection between agglomerates for the transport of protons through the catalyst layer. Moreover, oxygen should diffuse through the ionomer film in order to reach the active surface of catalyst particles. Thus, as ionomer film thickness (δ) increases it will effect proton conductivity positively through Eq. (3); however, at the same time it causes additional mass transfer resistance (Eq. (44)) for transport of oxygen from catalyst pores to agglomerate surface.

In Fig. 10, the polarization and power curves for three different values of δ (25, 50 and 100 nm) are plotted for constant values of remaining catalyst parameters. Fig. 10a indicates that at low current densities performance of the fuel cell is similar. Conversely, at high current densities (>0.7 A cm^{-2}) the fuel cell with higher δ (100 nm) suffers from mass transport losses caused by high value of ionomer film thickness. This effect is illustrated graphically in Fig. 11 in which percentage of the transport resistance caused by the ionomer film are given as a function of operating current density for different film thicknesses. As shown in Fig. 11, for all values

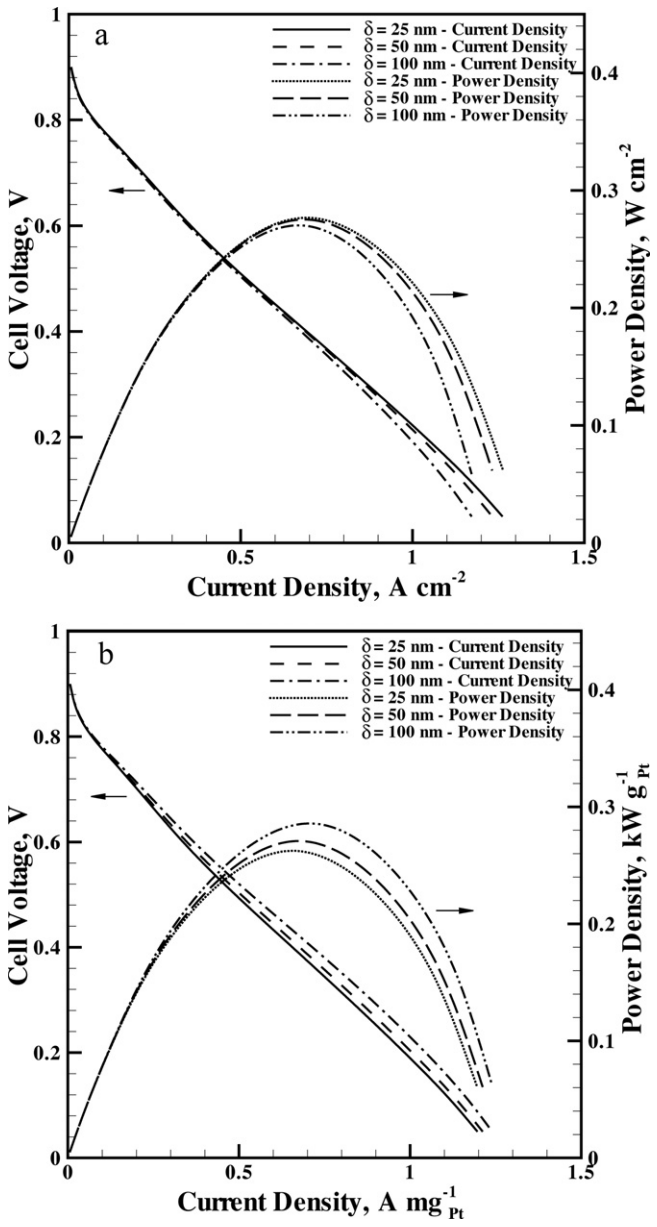

Fig. 10. Effect of ionomer film thickness (δ) on the fuel cell performance for r_{PtC} = 0.2, t_{cat} = 40 μm, r_{agg} = 2 μm, ε_{agg} = 0.3 and ε_{cat} = 0.2. (a) Polarization and power curves per unit MEA area and (b) polarization and power curves per unit platinum mass.

of film thicknesses, its contribution to total mass transfer resistance is relatively small at current densities lower than 0.5 A cm^{-2} which results in indistinguishable fuel cell performance in this region. However, at higher current densities (>0.5 A cm^{-2}) transport resistance due to polymer film starts to increase quickly for larger film thickness. It reaches nearly the half of the total transport resistance for the highest film thickness thereby reducing the performance of the cell. Meanwhile, for film thicknesses ≤50 nm, the resistance of the ionomer film is negligible even at higher current densities.

Fig. 10b shows that the fuel cell performance as current and power output per platinum loading increases with ionomer film thickness starting from low current densities. This performance improvement with δ is due to increase of total volume fraction polymer phase (Eq. (3)) and decrease of platinum loading of cathode catalyst layer when other catalyst parameters are constant. These results imply that increase of ionomer film thickness (δ) might

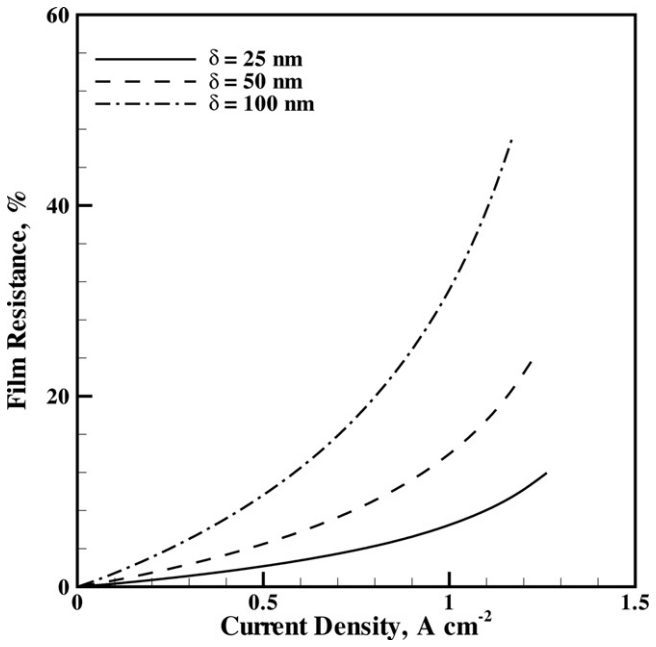

Fig. 11. Variation of average film resistance percentage in the cathode catalyst layer with polymer film thickness at various operating current densities for r_{PtC} = 0.2, t_{cat} = 40 μm, r_{agg} = 2 μm, ε_{agg} = 0.3 and ε_{cat} = 0.2.

cause increased mass transport resistances at higher current densities per unit area; however, at the same time, both the increase of total polymer phase volume fraction and the decrease of platinum loading might significantly enhance catalyst utilization as indicated by the polarization curves plotted for per unit mass of platinum loading.

3.2.6. Effect of catalyst layer porosity

Fig. 12 shows the variation of the performance of the fuel cell with cathode catalyst layer porosities of 0.1, 0.2 and 0.4. The key effect of porosity is on mass transport of oxygen through catalyst layer pores that is controlled by effective diffusion coefficient defined in Eq. (20). Thus, as porosity increases the diffusion of oxygen enhances, vice versa. On the other hand, the ionomer and platinum loading as well as solid and ionomer volume fractions of catalyst layer decreases as porosity of catalyst layer increases for constant value of the catalyst layer thickness. This change has an impact on both electron and proton transport in the catalyst layer through effective conductivity values determined by solid and ionomer void fractions of the catalyst layer (Eqs. (21) and (22)).

According to Fig. 12a, once the porosity of the catalyst layer increases the current and power densities per unit area of the fuel cell deteriorate. This implies that the effect of effective electron and proton conductivities is more significant than the effect of oxygen diffusion coefficient resulting in better performance for low values of ε_{cat}. Although the performance of the fuel cell per unit area decreases with ε_{cat}, opposite trend observed for current and power densities per unit mass. In this case, the improvement of oxygen transport in the catalyst layers with ε_{cat} counterbalance the reduction of platinum loading with ε_{cat} so that the performance of the cell increases (Fig. 12b). Therefore, for the present values of operating and catalyst parameters, larger catalyst layer porosity resulted in effective utilization of the catalyst loaded, thus larger mass specific power densities, however, at the same time lower current and power output per unit area obtained when ε_{cat} is high.

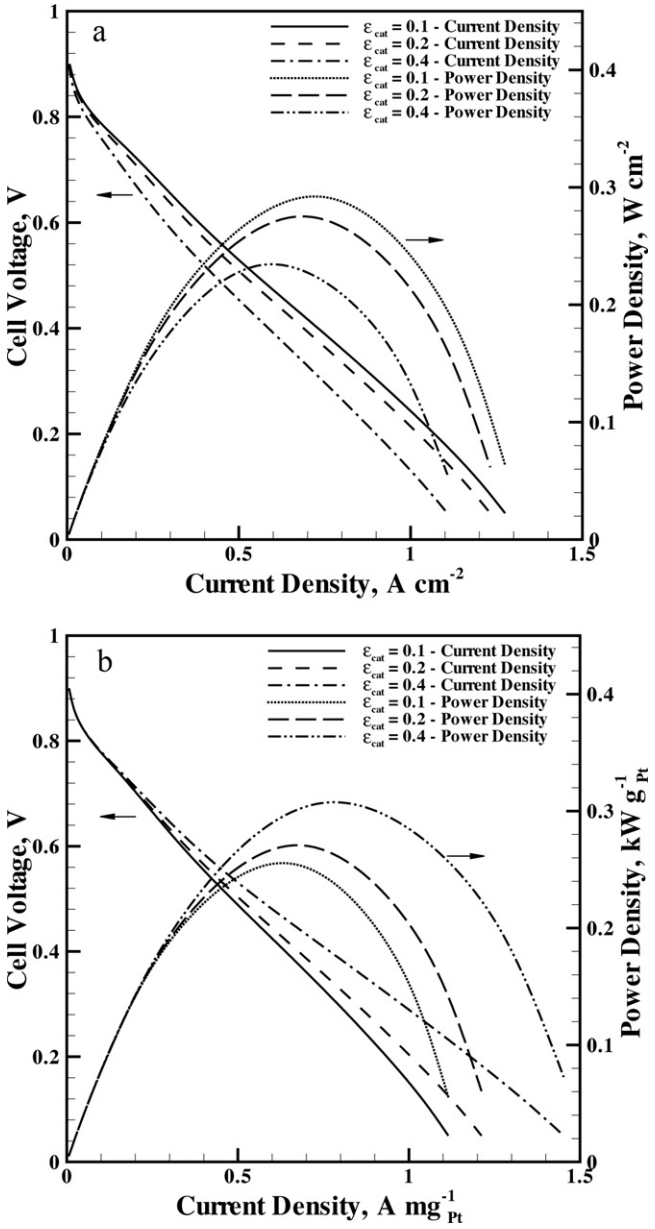

Fig. 12. Effect of the catalyst layer porosity (ε_{cat}) on the fuel cell performance for r_{PtC} = 0.2, t_{cat} = 40 μm, δ = 50 nm, r_{agg} = 2 μm and ε_{agg} = 0.3. (a) Polarization and power curves per unit MEA area and (b) polarization and power curves per unit platinum mass.

4. Conclusions

In this paper, a three-dimensional, non-isothermal, two-phase PEM fuel cell computational fluid dynamics model was presented and validated against the published experimental data. Ionomer film covered spherical agglomerate model was assumed for cathode catalyst layer. The effect of catalyst layer parameters such as platinum mass ratio of catalyst particles (r_{PtC}), catalyst layer thickness (t_{cat}), spherical agglomerate radius (r_{agg}), ionomer volume fraction inside an agglomerate (ε_{agg}), ionomer film thickness covering the agglomerates (δ) and catalyst layer porosity (ε_{cat}) on the PEM fuel cell performance were studied on three-dimensional geometry and for non-isothermal PEM fuel cell operation. According to the numerical results, the effect of these catalyst layer parameters on diffusion coefficients, electrical and proton conductivities as well as on effectiveness factor determines the area specific and platinum mass specific current and power densities of the PEM fuel cell separately. Thus, in the optimal design of a PEM fuel cell catalyst layer, one should first choose which type of power output (area specific or mass specific) is to be optimized. Then, depending on the requirements specified, optimal performance can be achieved by appropriately adjusting the parameters of the cathode catalyst layer.

References

[1] S.K. Das, A.S. Bansode, Heat Transfer Eng. 30 (2009) 691–719.
[2] T. Susai, A. Kawakami, A. Hamada, Y. Miyake, Y. Azegami, J. Power Sources 92 (2001) 131–138.
[3] W. Schmittinger, A. Vahidi, J. Power Sources 180 (2008) 1–14.
[4] J. Wu, X.Z. Yuan, J.J. Martin, H. Wang, J. Zhang, J. Shen, S. Wu, W. Merida, J. Power Sources 184 (2008) 104–119.
[5] S. Zhang, X. Yuan, H. Wang, W. Merida, H. Zhu, J. Shen, S. Wu, J. Zhang, Int. J. Hydrogen Energy 34 (2009) 388–404.
[6] W. Sun, B.A.P. Peppley, K. Karan, Electrochim. Acta 50 (2005) 3359–3374.
[7] K. Karan, Electrochem. Commun. 9 (2007) 747–753.
[8] N.P. Siegel, M.W. Ellis, D.J. Nelson, M.R. von Spakovsky, J. Power Sources 115 (2003) 81–89.
[9] Q. Wang, D. Song, T. Navessin, S. Holdcroft, Z. Liu, Electrochim. Acta 50 (2004) 725–730.
[10] R. Madhusudana Rao, Rengaswamy, J. Power Sources 158 (2006) 110–123.
[11] N.P. Siegel, M.W. Ellis, D.J. Nelson, M.R. von Spakovsky, J. Power Sources 128 (2004) 173–184.
[12] M. Secanell, K. Karan, A. Suleman, N. Djilali, Electrochim. Acta 52 (2007) 6318–6337.
[13] M. Secanell, B. Carnes, A. Suleman, N. Djilali, Electrochim. Acta 52 (2007) 2668–2682.
[14] C. Marr, X. Li, J. Power Sources 77 (1999) 17–27.
[15] L. You, H. Liu, Int. J. Hydrogen Energy 26 (2001) 991–999.
[16] C.Y. Du, G.P. Yin, X.Q. Cheng, P.F. Shi, J. Power Sources 160 (2006) 224–231.
[17] S.M. Rao, Y. Xing, J. Power Sources 185 (2008) 1094–1100.
[18] S. Kamarajugadda, S. Mazumder, J. Power Sources 183 (2008) 629–642.
[19] N. Khajeh-Hosseini-Dalasm, M.J. Kermani, D. Ghadiri Moghaddam, J.M. Stockie, Int. J. Hydrogen Energy 35 (2010) 2417–2427.
[20] Z. Zhang, L. Jia, Int. J. Energy Res. 33 (2009) 52–61.
[21] M. Secanell, Computational Modeling and Optimization of Proton Exchange Membrane Fuel Cells, PhD thesis, University of Victoria, 2007.
[22] G. Li, P.G. Pickup, J. Electrochem. Soc. 150 (2003) C742–C745.
[23] Q. Ye, T.V. Nguyen, J. Electrochem. Soc. 154 (2008) B1242–B1251.
[24] J.H. Nam, M. Kaviany, Int. J. Heat Mass Tran. 46 (2003) 4595–4611.
[25] T.E. Springer, T.A. Zawodzinski, S. Gottesfeld, J. Electrochem. Soc. 138 (1991) 2334–2342.
[26] S. Motupally, A.J. Becker, J.W. Weidner, J. Electrochem. Soc. 147 (2000) 3171–3177.
[27] H. Wu, X. Li, P. Berg, Electrochim. Acta 54 (2009) 6913–6927.
[28] M. Coppo, N.P. Siegel, M.R. von Spakovsky, J. Power Sources 159 (2006) 560–569.
[29] H.S. Fogler, Elements of Chemical Reaction Engineering, Prentice Hall Inc., New Jersey, 1999.
[30] A. Parthasarathy, S. Srinivasan, A.J. Appleby, C.R. Martin, J. Electrochem. Soc. 139 (1992) 2530–2537.
[31] A. Parthasarathy, S. Srinivasan, A.J. Appleby, C.R. Martin, J. Electrochem. Soc. 139 (1992) 2856–2862.
[32] F.W. He, J.S. Yi, T.V. Nguyen, AIChE J. 46 (2000) 2053–2064.
[33] A. Vorobev, O. Zikanov, T. Shamim, J. Power Sources 166 (2007) 92–103.
[34] J.T. Hinatsu, M. Mizuhata, H. Takenaka, J. Electrochem. Soc. 141 (1994) 1493–1498.
[35] L.M. Onishi, J.M. Prausnitz, J. Newman, J. Phys. Chem. B 111 (2007) 10166–10173.
[36] D. Cheddie, N. Munroe, J. Power Sources 147 (2005) 72–84.
[37] S.V. Patankar, Numerical Heat Transfer and Fluid Flow, Hemisphere Publishing Corporation, Washington, DC, 1980.
[38] W.R. Chang, J.J. Hwang, F.B. Weng, S.H. Chan, J. Power Sources 166 (2007) 149–154.
[39] R.F. Mann, J.C. Amphlett, B.A. Peppley, C.P. Thurgood, J. Power Sources 161 (2006) 768–774.
[40] J.P. Feser, A.K. Prasad, S.G. Advani, J. Power Sources 162 (2006) 1226–1231.
[41] J. Becker, R. Flückiger, M. Reum, F.N. Büchi, F. Marone, M. Stampanonic, J. Electrochem. Soc. 156 (2009) B1175–B1181.
[42] N. Zamel, X. Li, J. Shen, J. Becker, A. Wiegmann, Chem. Eng. Sci. 65 (2010) 3994–4006.
[43] M. Khandelwal, M.M. Mench, J. Power Sources 161 (2006) 1106–1115.
[44] J. Ramousse, O. Lottin, S. Didierjean, D. Maillet, J. Power Sources 192 (2009) 435–441.